Editors' Suggestion

Observation of Nodal-Line Plasmons in ZrSiS

Siwei Xue,[1,2] Maoyuan Wang,[3,4] Yong Li,[1,2] Shuyuan Zhang,[1] Xun Jia,[1] Jianhui Zhou,[5,*] Youguo Shi,[1,6] Xuetao Zhu,[1,2,6,†] Yugui Yao,[3] and Jiandong Guo[1,2,6,7,‡]

[1]*Beijing National Laboratory for Condensed Matter Physics and Institute of Physics, Chinese Academy of Sciences, Beijing 100190, China*

[2]*School of Physical Sciences, University of Chinese Academy of Sciences, Beijing 100049, China*

[3]*Key Laboratory of Advanced Optoelectronic Quantum Architecture and Measurement (MOE), School of Physics, Beijing Institute of Technology, Beijing 100081, China*

[4]*International Center for Quantum Materials, School of Physics, Peking University, Beijing 100871, China*

[5]*Anhui Province Key Laboratory of Condensed Matter Physics at Extreme Conditions, High Magnetic Field Laboratory, HFIPS, Chinese Academy of Sciences, Hefei 230031, China*

[6]*Songshan Lake Materials Laboratory, Dongguan, Guangdong 523808, China*

[7]*Collaborative Innovation Center of Quantum Matter, Beijing 100871, China*

(Received 5 March 2021; accepted 27 September 2021; published 26 October 2021)

Nodal-line semimetals (NLSMs), a large family of new topological phases of matter with continuous linear band crossing points in the momentum space, attract considerable attention. Here, we report the direct observation of plasmons originating from topological nodal-line states in a prototypical NLSM ZrSiS by high-resolution electron energy loss spectroscopy. There exist three temperature-independent plasmons with energies ranging from the near- to the mid-infrared frequencies. With first-principles calculations of a slab model, these plasmons can be ascribed to the correlations of electrons in the bulk nodal lines and their projected surface states, dubbed nodal-line plasmons. An anomalous surface plasmon has higher excitation energy than the bulk plasmon due to the larger contribution from the nodal-line projected surface states. This work reveals the novel plasmons related to the unique nodal-line states in a NLSM.

DOI: 10.1103/PhysRevLett.127.186802

Introduction.—Topological materials, including topological insulators and topological semimetals, possess topologically nontrivial bulk states and surface states [1–6]. Recently, a series of fascinating plasmons in topological materials [7–20] have been predicted, such as the spin plasmon [8], the chirality-anomaly induced plasmon [12], and the tilting induced undamped gapless plasmon [20]. Meanwhile, many unconventional bulk and surface plasmons have been observed in topological materials through high-resolution electron energy loss spectroscopy (HREELS) [21–25] and optical spectroscopy [26–29]. However, most of the previous studies mainly focused on the topological insulators and topological semimetals with discrete band crossing points (Dirac or Weyl points) and the resulting low-density mobile Dirac electrons.

Instead of the discrete crossing points, topological materials with one-dimensional continuous linear band crossing points in the momentum space are classified into the so-called nodal-line semimetals (NLSMs) [30,31]. A great number of candidate materials have been predicted [32–41] and exhibited many novel physical properties from the unique nodal-line electronic structures [42–51]. The topological nodal-line states contribute much larger Fermi surfaces to both the surface and bulk Brillouin zones. Consequently, the nodal-line Fermi surfaces and the corresponding high carrier density could significantly influence the plasmon excitations [52,53]. Here, we would like to take a realistic NLSM ZrSiS as a prototype to demonstrate the important impacts of topological nodal lines on plasmons.

In this Letter, we observe three monotonously dispersing plasmons (α, β, and γ) in ZrSiS by HREELS. Theoretical calculations suggest their origins from the intra- or interband correlations of bulk nodal lines and their projected surface states. Remarkably, the surface γ plasmon has higher excitation energy than the bulk β plasmon due to the larger contribution from the nodal-line projected surface states. Moreover, the energy dispersions of all these plasmons in ZrSiS are temperature-independent, distinct from the plasmons in other known semimetals.

Electronic properties of ZrSiS.—ZrSiS crystallizes in a tetragonal lattice whose space group is $P4/nmm$ (No. 129) and point group D_{4h}, with Si square nets sandwiched by Zr-S layers [Fig. 1(a)]. The weak bonding between two adjacent Zr-S layers makes it easy to cleave along the (001) plane. With the aid of low-energy electron diffraction (LEED), a (1×1) square lattice is clearly observed [Fig. 1(b)], confirming the tetragonal structure and the cleaved (001) crystal plane. There are two nonsymmorphic symmetries in the crystal structure, a glide mirror plane and

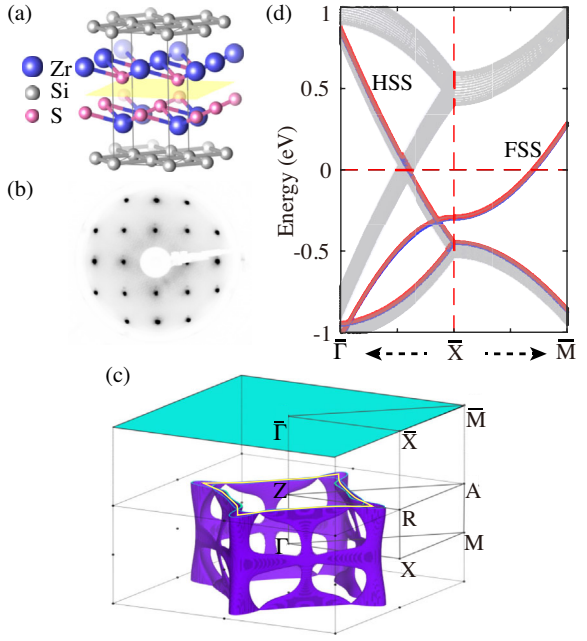

FIG. 1. (a) Crystal structure of ZrSiS with thin solid lines depicting a unit cell and yellow plane representing the cleavage plane. (b) LEED pattern on the (001) surface of ZrSiS, obtained at room temperature with an incident beam energy of 125 eV. (c) Fermi surface in the bulk Brillouin zone encapsulating nodal lines in electron or hole pockets. The diamondlike nodal line at $k_z = \pi$ plane is demonstrated by the yellow lines as an example. The cyan plane above is the surface Brillouin zone. (d) Band structures of ZrSiS along the $\bar{\Gamma}\,\bar{X}\,\bar{M}$ path around $\bar{X}$ point from the tight-binding model. The gray lines are the projection of bulk bands, while the blue and red lines are the surface states (the HSS and the FSS, with the details in the text).

two screw axes $C_{2x}(C_{2y})$. The crossing of the conduction band and valence band near the Fermi energy is along a continuous trajectory in the momentum space [33,54–56]. The bands around the line nodes disperse linearly in a large energy range (about 0.5 eV) without overlapping with other bands [33,54,56–60]. Our calculations (Fig. S8 in the Supplemental Material (SM) [61]) reproduce the bulk electronic bands reported in other works [33,56].

NLSMs are predicted to possess topological drumhead-like surface states [31,40]. But such drumheadlike surface states in ZrSiS still lack experimental evidence. In fact, when the bulk nodal lines are projected onto the surface, hybrid surface states (HSS) will appear on the upper edge of the projected bands [Fig. 1(d), with a detailed model in Sec. III A of the SM [61]]. Moreover, the breaking of the nonsymmorphic symmetries at the cleaved surface leads to the floating surface states (FSS) [Fig. 1(d)] that are distinct from the conventional Shockley states, quantum well states, or topologically protected surface states [70]. In this context, the intraband and interband correlations among the three different kinds of electronic states (bulk nodal line, HSS, and FSS) would give rise to rich plasmon properties in ZrSiS.

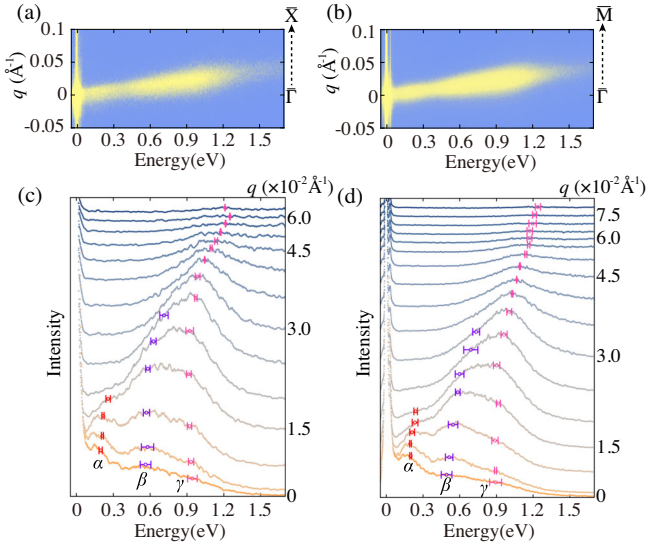

FIG. 2. Typical 2D momentum-energy mappings of HREELS along (a) the $\bar{\Gamma}\,\bar{X}$ and (b) the $\bar{\Gamma}\,\bar{M}$ directions of ZrSiS at room temperature. (c),(d) Stacks of momentum-dependent EDCs along the $\bar{\Gamma}\,\bar{X}$ and $\bar{\Gamma}\,\bar{M}$ directions, respectively. The corresponding momentum values are listed on the right. The plasmon peak positions are indicated, with error bars from the fitting procedure described in the text.

Plasmons from HREELS.—The plasmon dispersions of ZrSiS were measured by a HREELS system with the capability of 2D energy and momentum mapping [71]. The excitation spectra detected along the $\bar{\Gamma}\,\bar{X}$ and $\bar{\Gamma}\,\bar{M}$ directions with incident energy $E_i = 110$ eV are illustrated in Figs. 2(a) and 2(b), respectively. In the 2D mapping, the yellow represents the distribution of the energy loss, with zero energy corresponding to the elastic scattering and nonzero features corresponding to the collective excitations of ZrSiS. Some fine structures can be identified below 50 meV, which are the phonons discussed previously [72]. Besides, there are several noticeable energy loss features between 0.1 eV and 1.5 eV. To understand these features, we extract the momentum-dependent energy distribution curves (EDCs) along $\bar{\Gamma}\,\bar{X}$ and $\bar{\Gamma}\,\bar{M}$ directions, as plotted in Figs. 2(c) and 2(d), respectively. From the EDCs, three energy loss peaks, labeled α, β, and γ, can be clearly discerned, especially in the small momentum range. To quantitatively obtain the plasmon dispersions, the peaks were fitted by Gaussian functions with the Drude background subtracted (see details in the SM [61]). The extracted energy dispersions and linewidths are shown in Figs. 3(a) and 3(b), respectively. The excitation energy of α plasmon is ~0.20 eV at $q = 0$, dispersing to ~0.26 eV at $q \sim 0.02$ Å^{-1}, and damps out quickly beyond $q \sim 0.02$ Å^{-1}. The β and γ plasmons show similar energy dispersions and damping behaviors. We summarize their energy ranges in Table I. Figure 3(a) also suggests that the overall dispersions of all of the three plasmons along the

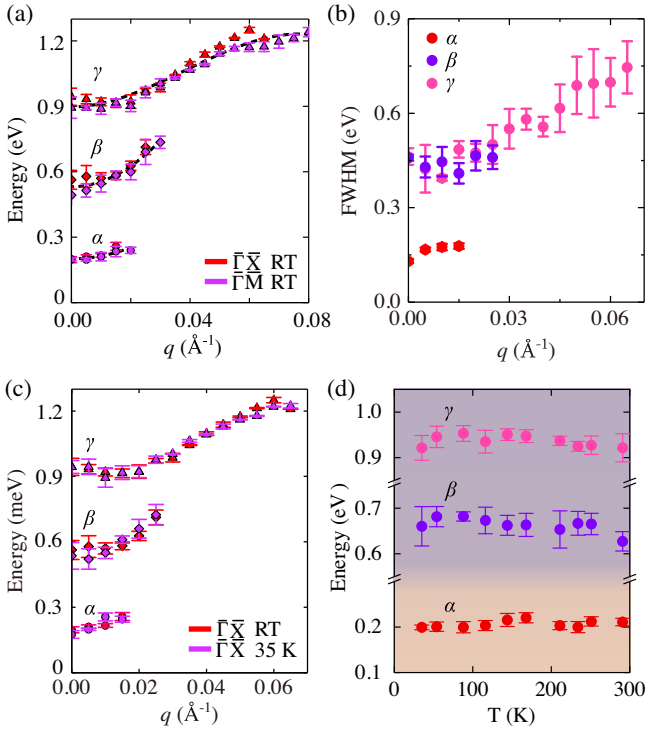

FIG. 3. (a) Extracted plasmon dispersions from the EDC stacks in Figs. 2. The dashed lines are the polynomial fittings. (b) Extracted plasmon linewidths (full width at half maximum, FWHM) along the $\bar{\Gamma}\bar{X}$ direction at room temperature (RT). (c) Comparison of dispersions along the $\bar{\Gamma}\bar{X}$ direction between RT and 35 K. (d) The dependence of peak positions on temperature. The peak positions of α are at $q = 0.005$ Å^{-1} while the peak positions of β and γ are at $q = 0.020$ Å^{-1}. The error bars originate from the uncertainty of the fittings with different background subtractions.

two high symmetry directions ($\bar{\Gamma}\bar{X}$ and $\bar{\Gamma}\bar{M}$) are identical. It is theoretically predicted that plasmon dispersions are anisotropic along the directions parallel and perpendicular to the nodal-line plane [52]. However, the nodal lines in ZrSiS show complicated distributions in the 3D Brillouin zone [Fig. 1(c)]. And thus the missing anisotropy at the two directions in the surface Brillouin zone cannot fully reflect the direction-dependent information.

Moreover, we also performed the temperature-dependent HREELS measurements (details in Sec. II D of the SM [61]). The plasmon dispersions at 35 K and at room temperature are both plotted in Fig. 3(c), and several typical peak positions at different temperatures are plotted in Fig. 3(d). It is known that the thermally excited carriers in semimetals usually lead to a strongly temperature-dependent plasmon frequency, such as in graphite [73] and in 3D Dirac and Weyl semimetals [13,14,24,74]. However, the energy dispersions of the observed plasmons in ZrSiS are all temperature independent, a typical behavior resembling well-defined metallic plasmons.

TABLE I. Summary of the observed plasmons in ZrSiS.

Plasmon	Energy (eV)	Origin
α	0.20–0.26	Interband correlations between FSS and HSS
β	0.50–0.75	Intraband correlations within bulk nodal lines
γ	0.90–1.18	Intraband correlations within HSS

Origin of plasmons.—To elucidate the nature of the measured plasmons, we first briefly discuss the possible plasmons from the modeled electronic structure in Fig. 1(d). First of all, the intraband correlations within the linearly dispersing bulk nodal-line bands around the Fermi surface usually support a bulk plasmon. Second, the intraband correlations within the surface states crossing the Fermi level (HSS) will generate a surface plasmon. Third, the interband correlations between the HSSs and the FSSs would strongly modify the surface plasmons and may generate an extra surface plasmon. Note that other band correlations make minor contributions to measured plasmons and can be ignored [75].

In order to gain quantitative understanding of the plasmons, we carry out first-principles calculations for the plasmon dispersions. The plasmons can be revealed as sharp peaks in the electron energy-loss functions [76]

$$L(\mathbf{q},\omega) = \mathrm{Im}\left[\frac{-1}{\varepsilon^{(\mathrm{RPA})}(\mathbf{q},\omega)}\right], \tag{1}$$

and the dynamical dielectric functions within the random phase approximation (RPA) are given as [77]

$$\varepsilon^{(\mathrm{RPA})}(\mathbf{q},\omega) = 1 - v_q \Pi(\mathbf{q},\omega), \tag{2}$$

where $\Pi(\mathbf{q},\omega)$ is the density-density correlation function and v_q is the 3D Coulomb interaction.

Since HREELS mainly probes the signals from the topmost few layers, we thus consider a 20-layer slab [Fig. 4(a)] terminated with a S-atom surface to calculate the layer-dependent dielectric functions as well as the energy-loss functions [78]. The calculated electronic band structure is shown in Fig. 4(b). The projected nodal-line bands and the surface states from the slab calculations are well consistent with the bands from the tight-binding model in Fig. 1(d). Using Eqs. (1) and (2), three plasmons were obtained. We ascribe the peak of each plasmon mode to the intraband or interband correlations of the bulk or the surface states. We could assign the most relevant processes for electron-hole excitations that dominate each plasmon mode (Fig. S10 in the SM [61]). The comparison with the experimental results, shown in Fig. 4(c), can reveal the origin of the measured plasmons. The β plasmon with the energy around 0.6 eV, is dominated by the intraband correlations of the bulk nodal-line electrons around the

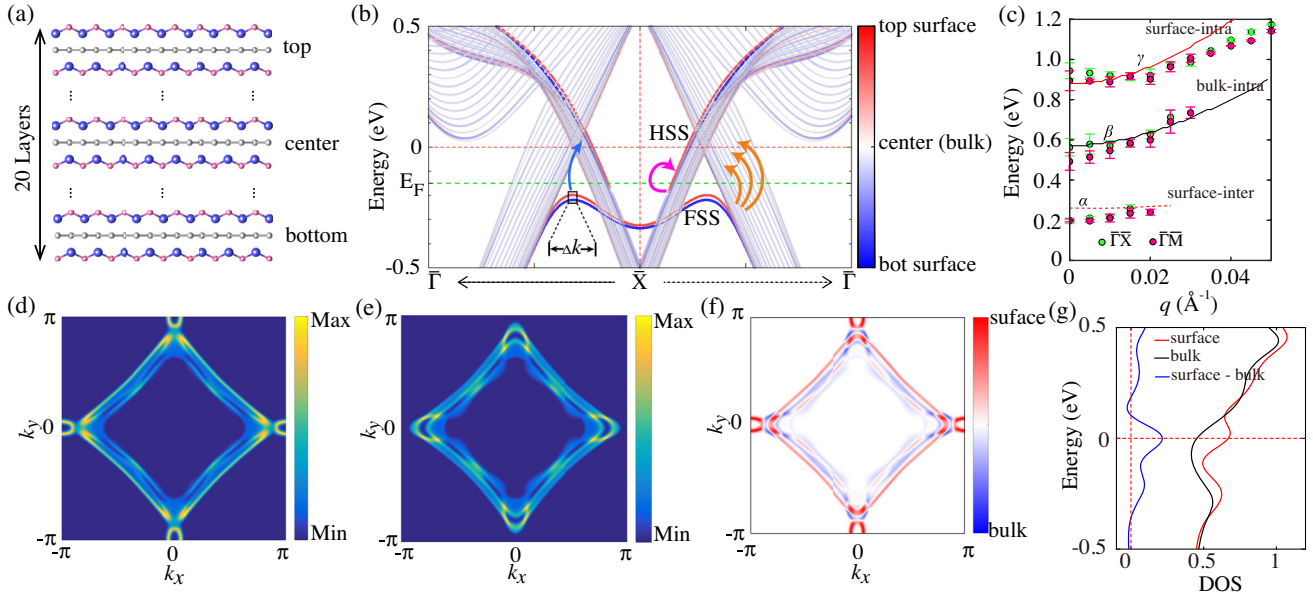

FIG. 4. (a) Schematic for the slab of ZrSiS for the DFT calculations. (b) Calculated electronic dispersions of the slab in (a) along the $\bar{\Gamma}$-$\bar{X}$-$\bar{\Gamma}$ path around $\bar{X}$ point. The gray solid lines are the surface projected bulk bands. The color bar indicates the position of the surface states in the slab. The green dashed line is the position of the experimental Fermi level obtained from ARPES. The blue arrow sketches the interband correlations between the HSSs and the FSSs, while the pink (orange) arrows correspond to the intraband correlations within the HSSs (within the projected nodal-line bands). (c) Comparison between the experimental plasmon peaks (dots) and the calculated loss functions (lines). (d),(e) The calculated Fermi surface at surface and center of the slab in (a), respectively. (f) Difference between (d) and (e). The red means the surface density is larger than the bulk one, and blue means the opposite. (g) The local density of states (DOS) of slab with red, black, and blue curves for surface, bulk, and their difference, respectively.

Fermi surface, which was simulated at the slab center. The α plasmon with the energy around 0.3 eV and the γ plasmon with the energy around 1.0 eV are both related to the surface states, which are simulated at the top or bottom surface of the slab. It turns out that the α plasmon comes from the interband correlations between the HSS and the FSS, while the γ plasmon is from the intraband correlations within the HSS. As explained in the SM [61], the HSS and the FSS are both the projected surface states from the bulk nodal lines. As a result, all three plasmons originate from the nodal-line states and can be dubbed as nodal-line plasmons. The origins of these plasmons are listed in Table I.

The dispersions of these plasmons can be fitted by simple polynomial functions

$$\omega(q) = \omega_0 + Cq^2 + Dq^3, \tag{3}$$

where ω_0 represents the plasmon energy at $q = 0$, and C and D are the fitting parameters. The fitting results are plotted in Fig. 3(a). The nearly flat band of α plasmon reflects the nature of its interband correlations. The dispersion of the β plasmon is parabolic, manifesting its bulk nature, which is consistent with the predicted bulk plasmon dispersion of NLSMs [52]. The dispersion of the γ plasmon is parabolic at small q while deviates from the parabola with a cubic term at large q, reminiscent of the plasmon dispersions at the surface of simple metals [79].

Interestingly, the excitation energy of the surface intraband plasmon γ is much higher than that of the bulk intraband plasmon β. It can be understood by comparing the Fermi surfaces at different positions in the slab. The Fermi surface obtained at the top (bottom) of the slab [Fig. 4(d)] occupies a larger area in the k_x-k_y plane than the one obtained at the center [Fig. 4(e)], which can be confirmed by the difference of the two images, shown in Fig. 4(f). The local density of states (DOS) around the Fermi energy at the surface and at the center of the slab are plotted in Fig. 4(g), indicating that the local DOS at the slab surface is larger than that at the slab center. It can be verified from Figs. 4(f) and 4(g) that the surface has larger carrier density than the bulk,which is responsible for the higher excitation energy of the γ plasmon compared with that of the β plasmon. Note that the γ plasmon is mainly induced by the HSS which is a hybrid of surface and bulk states, instead of the purely 2D FSS. Therefore the γ plasmon does not obey the 2D characteristic $\sqrt{q}$ law. Note that this anomalous enhancement of excitation energy of surface plasmon is unique and absent in 3D electron gases and Dirac and Weyl semimetals.

The nature of interband correlations of the α plasmon can also be analyzed from Fig. 4(g). Two peaks around 0 eV and -0.25 eV clearly appear in the surface DOS, implying the strong interband correlations. The peak at -0.25 eV is dominated by the FSS, while the peak at 0 eV is dominated

by the linear HSS, as illustrated in Fig. 4(b). The length of the FSS with the largest DOS is relatively short [$\Delta k \sim 0.02$ Å^{-1} in Fig. 4(b)] compared to the size of the Brillouin zone, which accounts for a narrow window to observe the α plasmon ($q < 0.02$ Å^{-1}) [Fig. 3(a)]. The calculated Im[ε], shown in Sec. III C of the SM [61], verifies that the α plasmon indeed damps out beyond $q > 0.025$ Å^{-1}.

The above calculations within RPA well capture the three measured plasmons and their energy dispersions. However, as shown in Fig. 4(c), the calculated energy dispersions, especially for the γ plasmon at large q, deviate from the experimental results. This discrepancy is mainly due to the electron-electron correlations beyond the RPA, leading to inaccuracy in the large momentum regime. The strong correlation interactions [45] in ZrSiS have been manifested by the unconventional mass enhancement of carriers [44]. Especially, the surface states in ZrSiS are mostly composed of d electrons, which have strong local field effects that will influence the plasmon behavior [77]. Similarly, the correlation and local field effects would also modify the electron-hole continuum and account for the disappearance of the β plasmon at large q. In addition, the damping channels due to scatterings by impurities and phonons are neglected in the RPA calculations. Therefore, these aspects call for a comprehensive theory to fully capture the damping behaviors of the observed plasmons.

To summarize, we have observed three plasmons (α, β, and γ) and revealed their nature from the nodal-line states and the related surface states in ZiSiS. An anomalous surface plasmon γ has higher excitation energy than the bulk plasmon β due to the larger contribution from the nodal-line projected surface states. All of the observed plasmons are temperature independent, providing possibilities for plasmonics or optics with high thermal stability [80,81].

This work was supported by the National Natural Science Foundation of China (No. 11874404, No. 11634016, No. 11734003, No. 12061131002, No. 12174394, and No. U2032204), the National Key R&D Program of China (No. 2016YFA0302400, No. 2016YFA0202300, No. 2017YFA0303600, and No. 2020YFA0308800), and the Strategic Priority Research Program of Chinese Academy of Sciences (No. XDB33000000 and No. XDB28000000). M. W. was supported by the National Basic Research Program of China (Grant No. 2015CB921102). X. Z. was partially supported by the Youth Innovation Promotion Association of Chinese Academy of Sciences (No. 2016008). J. Z. was supported by the High Magnetic Field Laboratory of Anhui Province. Y. S. was supported by the Beijing Natural Science Foundation (Z180008), and the K. C. Wong Education Foundation (GJTD-2018-01).

S. X., M. W., and Y. L. contributed equally to this work.

*jhzhou@hmfl.ac.cn
†xtzhu@iphy.ac.cn
‡jdguo@iphy.ac.cn

[1] M. Z. Hasan and C. L. Kane, Colloquium: Topological insulators, Rev. Mod. Phys. **82**, 3045 (2010).
[2] X.-L. Qi and S.-C. Zhang, Topological insulators and superconductors, Rev. Mod. Phys. **83**, 1057 (2011).
[3] B. Yan and C. Felser, Topological materials: Weyl semimetals, Annu. Rev. Condens. Matter Phys. **8**, 337 (2017).
[4] N. P. Armitage, E. J. Mele, and A. Vishwanath, Weyl and dirac semimetals in three-dimensional solids, Rev. Mod. Phys. **90**, 015001 (2018).
[5] H. Gao, J. W. Venderbos, Y. Kim, and A. M. Rappe, Topological semimetals from first principles, Annu. Rev. Mater. Res. **49**, 153 (2019).
[6] X. Chen, J. Liu, and J. Li, Topological phononic materials: Computation and data, The Innovation **2**, 100134 (2021).
[7] S. Das Sarma and E. H. Hwang, Collective Modes of the Massless Dirac Plasma, Phys. Rev. Lett. **102**, 206412 (2009).
[8] S. Raghu, S. B. Chung, X.-L. Qi, and S.-C. Zhang, Collective Modes of a Helical Liquid, Phys. Rev. Lett. **104**, 116401 (2010).
[9] A. Karch, Surface plasmons and topological insulators, Phys. Rev. B **83**, 245432 (2011).
[10] M. Lv and S.-C. Zhang, Dielectric functions, Friedel oscillation and plasmons in Weyl semimetals, Int. J. Mod. Phys. B **27**, 1350177 (2013).
[11] S. Juergens, P. Michetti, and B. Trauzettel, Plasmons due to the Interplay of Dirac and Schrödinger Fermions, Phys. Rev. Lett. **112**, 076804 (2014).
[12] J. Zhou, H.-R. Chang, and D. Xiao, Plasmon mode as a detection of the chiral anomaly in Weyl semimetals, Phys. Rev. B **91**, 035114 (2015).
[13] J. Hofmann and S. Das Sarma, Plasmon signature in Dirac-Weyl liquids, Phys. Rev. B **91**, 241108(R) (2015).
[14] D. E. Kharzeev, R. D. Pisarski, and H.-U. Yee, Universality of Plasmon Excitations in Dirac Semimetals, Phys. Rev. Lett. **115**, 236402 (2015).
[15] J. C. W. Song and M. S. Rudner, Fermi arc plasmons in Weyl semimetals, Phys. Rev. B **96**, 205443 (2017).
[16] F. Zhang, J. Zhou, D. Xiao, and Y. Yao, Tunable Intrinsic Plasmons due to Band Inversion in Topological Materials, Phys. Rev. Lett. **119**, 266804 (2017).
[17] E. V. Gorbar, V. A. Miransky, I. A. Shovkovy, and P. O. Sukhachov, Consistent Chiral Kinetic Theory in Weyl Materials: Chiral Magnetic Plasmons, Phys. Rev. Lett. **118**, 127601 (2017).
[18] G. M. Andolina, F. M. D. Pellegrino, F. H. L. Koppens, and M. Polini, Quantum nonlocal theory of topological Fermi arc plasmons in Weyl semimetals, Phys. Rev. B **97**, 125431 (2018).
[19] J. Wang, X. Sui, S. Gao, W. Duan, F. Liu, and B. Huang, Anomalous Dirac Plasmons in 1D Topological Electrides, Phys. Rev. Lett. **123**, 206402 (2019).
[20] K. Sadhukhan, A. Politano, and A. Agarwal, Novel Undamped Gapless Plasmon Mode in a Tilted Type-II Dirac Semimetal, Phys. Rev. Lett. **124**, 046803 (2020).
[21] A. Politano, V. M. Silkin, I. A. Nechaev, M. S. Vitiello, L. Viti, Z. S. Aliev, M. B. Babanly, G. Chiarello,

P. M. Echenique, and E. V. Chulkov, Interplay of Surface and Dirac Plasmons in Topological Insulators: The Case of Bi_2Se_3, Phys. Rev. Lett. **115**, 216802 (2015).

[22] A. Politano, G. Chiarello, B. Ghosh, K. Sadhukhan, C.-N. Kuo, C. S. Lue, V. Pellegrini, and A. Agarwal, 3D Dirac Plasmons in the Type-II Dirac Semimetal $PtTe_2$, Phys. Rev. Lett. **121**, 086804 (2018).

[23] X. Jia, S. Zhang, R. Sankar, F.-C. Chou, W. Wang, K. Kempa, E. W. Plummer, J. Zhang, X. Zhu, and J. Guo, Anomalous Acoustic Plasmon Mode from Topologically Protected States, Phys. Rev. Lett. **119**, 136805(2017).

[24] X. Jia, M. Wang, D. Yan, S. Xue, S. Zhang, J. Zhou, Y. Shi, X. Zhu, Y. Yao, and J. Guo, Topologically nontrivial interband plasmons in type-II Weyl semimetal $MoTe_2$, New J. Phys. **22**, 103032 (2020).

[25] A. Kogar, S. Vig, A. Thaler, M. H. Wong, Y. Xiao, D. Reig-i Plessis, G. Y. Cho, T. Valla, Z. Pan, J. Schneeloch, R. Zhong, G. D. Gu, T. L. Hughes, G. J. MacDougall, T.-C. Chiang, and P. Abbamonte, Surface Collective Modes in the Topological Insulators Bi_2Se_3 and $Bi_{0.5}Sb_{1.5}Te_{3-x}Se_x$, Phys. Rev. Lett. **115**, 257402 (2015).

[26] P. Di Pietro, M. Ortolani, O. Limaj, A. Di Gaspare, V. Giliberti, F. Giorgianni, M. Brahlek, N. Bansal, N. Koirala, S. Oh, P. Calvani, and S. Lupi, Observation of Dirac plasmons in a topological insulator, Nat. Nanotechnol. **8**, 556 (2013).

[27] P. Venuthurumilli, X. Wen, V. Iyer, Y. P. Chen, and X. Xu, Near-field imaging of surface plasmons from the bulk and surface state of topological insulator Bi_2Te_2Se, ACS Photonics **6**, 2492 (2019).

[28] Y. D. Glinka, S. Babakiray, T. A. Johnson, M. B. Holcomb, and D. Lederman, Nonlinear optical observation of coherent acoustic Dirac plasmons in thin-film topological insulators, Nat. Commun. **7**, 13054 (2016).

[29] C. Wang, Y. Sun, S. Huang, Q. Xing, G. Zhang, C. Song, F. Wang, Y. Xie, Y. Lei, Z. Sun, and H. Yan, Tunable Plasmons in Large-Area WTe_2 Thin Films, Phys. Rev. Applied **15**, 014010 (2021).

[30] A. A. Burkov, M. D. Hook, and L. Balents, Topological nodal semimetals, Phys. Rev. B **84**, 235126 (2011).

[31] C. Fang, Y. Chen, H.-Y. Kee, and L. Fu, Topological nodal line semimetals with and without spin-orbital coupling, Phys. Rev. B **92**, 081201(R) (2015).

[32] R. Li, H. Ma, X. Cheng, S. Wang, D. Li, Z. Zhang, Y. Li, and X.-Q. Chen, Dirac Node Lines in Pure Alkali Earth Metals, Phys. Rev. Lett. **117**, 096401 (2016).

[33] L. M. Schoop, M. N. Ali, C. Straßer, A. Topp, A. Varykhalov, D. Marchenko, V. Duppel, S. S. P. Parkin, B. V. Lotsch, and C. R. Ast, Dirac cone protected by non-symmorphic symmetry and three-dimensional Dirac line node in ZrSiS, Nat. Commun. **7**, 11696 (2016).

[34] J. Hu, Z. Tang, J. Liu, X. Liu, Y. Zhu, D. Graf, K. Myhro, S. Tran, C. N. Lau, J. Wei, and Z. Mao, Evidence of Topological Nodal-Line Fermions in ZrSiSe and ZrSiTe, Phys. Rev. Lett. **117**, 016602 (2016).

[35] S. Li, Y. Liu, S.-S. Wang, Z.-M. Yu, S. Guan, X.-L. Sheng, Y. Yao, and S. A. Yang, Nonsymmorphic-symmetry-protected hourglass Dirac loop, nodal line, and Dirac point in bulk and monolayer X_3SiTe_6 (X = Ta, Nb), Phys. Rev. B **97**, 045131 (2018).

[36] B. Feng, B. Fu, S. Kasamatsu, S. Ito, P. Cheng, C.-C. Liu, Y. Feng, S. Wu, S. K. Mahatha, P. Sheverdyaeva, P. Moras, M. Arita, O. Sugino, T.-C. Chiang, K. Shimada, K. Miyamoto, T. Okuda, K. Wu, L. Chen, Y. Yao, and I. Matsuda, Experimental realization of two-dimensional Dirac nodal line fermions in monolayer Cu_2Si, Nat. Commun. **8**, 1007 (2017).

[37] X.-B. Wang, X.-M. Ma, E. Emmanouilidou, B. Shen, C.-H. Hsu, C.-S. Zhou, Y. Zuo, R.-R. Song, S.-Y. Xu, G. Wang, L. Huang, N. Ni, and C. Liu, Topological surface electronic states in candidate nodal-line semimetal CaAgAs, Phys. Rev. B **96**, 161112(R) (2017).

[38] Z. Liu, R. Lou, P. Guo, Q. Wang, S. Sun, C. Li, S. Thirupathaiah, A. Fedorov, D. Shen, K. Liu, H. Lei, and S. Wang, Experimental Observation of Dirac Nodal Links in Centrosymmetric Semimetal TiB_2, Phys. Rev. X **8**, 031044 (2018).

[39] R. Lou, P. Guo, M. Li, Q. Wang, Z. Liu, S. Sun, C. Li, X. Wu, Z. Wang, Z. Sun, D. Shen, Y. Huang, K. Liu, Z.-Y. Lu, H. Lei, H. Ding, and S. Wang, Experimental observation of bulk nodal lines and electronic surface states in ZrB_2, npj Quantum Mater. **3**, 43 (2018).

[40] R. Yu, Z. Fang, X. Dai, and H. Weng, Topological nodal line semimetals predicted from first-principles calculations, Front. Phys. **12**, 92 (2017).

[41] Y. Shao, Z. Sun, Y. Wang, C. Xu, R. Sankar, A. J. Breindel, C. Cao, M. M. Fogler, A. J. Millis, F. Chou, Z. Li, T. Timusk, M. B. Maple, and D. N. Basov, Optical signatures of Dirac nodal lines in $NbAs_2$, Proc. Natl. Acad. Sci. U.S.A. **116**, 1168 (2019).

[42] K. Mullen, B. Uchoa, and D. T. Glatzhofer, Line of Dirac Nodes in Hyperhoneycomb Lattices, Phys. Rev. Lett. **115**, 026403 (2015).

[43] J.-W. Rhim and Y. B. Kim, Landau level quantization and almost flat modes in three-dimensional semimetals with nodal ring spectra, Phys. Rev. B **92**, 045126 (2015).

[44] S. Pezzini, M. R. van Delft, L. M. Schoop, B. V. Lotsch, A. Carrington, M. I. Katsnelson, N. E. Hussey, and S. Wiedmann, Unconventional mass enhancement around the Dirac nodal loop in ZrSiS, Nat. Phys. **14**, 178 (2018).

[45] Y. Huh, E.-G. Moon, and Y. B. Kim, Long-range Coulomb interaction in nodal-ring semimetals, Phys. Rev. B **93**, 035138 (2016).

[46] A. N. Rudenko, E. A. Stepanov, A. I. Lichtenstein, and M. I. Katsnelson, Excitonic Instability and Pseudogap Formation in Nodal Line Semimetal ZrSiS, Phys. Rev. Lett. **120**, 216401 (2018).

[47] W. Chen, H.-Z. Lu, and O. Zilberberg, Weak Localization and Antilocalization in Nodal-Line Semimetals: Dimensionality and Topological Effects, Phys. Rev. Lett. **122**, 196603 (2019).

[48] N.-X. Yang, Z. Hou, and Q.-F. Sun, Plateaus of quantized conductance with high steps in topological nodal-line semimetals, Phys. Rev. B **101**, 035418 (2020).

[49] F. C. Chen, Y. Fei, S. J. Li, Q. Wang, X. Luo, J. Yan, W. J. Lu, P. Tong, W. H. Song, X. B. Zhu, L. Zhang, H. B. Zhou, F. W. Zheng, P. Zhang, A. L. Lichtenstein, M. I. Katsnelson, Y. Yin, N. Hao, and Y. P. Sun, Temperature-Induced Lifshitz

Transition and Possible Excitonic Instability in ZrSiSe, Phys. Rev. Lett. **124**, 236601 (2020).
[50] M. Gonçalves, P. Ribeiro, E. V. Castro, and M. A. N. Araújo, Disorder-Driven Multifractality Transition in Weyl Nodal Loops, Phys. Rev. Lett. **124**, 136405 (2020).
[51] J. Liu and L. Balents, Correlation effects and quantum oscillations in topological nodal-loop semimetals, Phys. Rev. B **95**, 075426 (2017).
[52] J.-W. Rhim and Y. B. Kim, Anisotropic density fluctuations, plasmons, and Friedel oscillations in nodal line semimetal, New J. Phys. **18**, 043010 (2016).
[53] Z. Yan, P.-W. Huang, and Z. Wang, Collective modes in nodal line semimetals, Phys. Rev. B **93**, 085138 (2016).
[54] B.-B. Fu, C.-J. Yi, T.-T. Zhang, M. Caputo, J.-Z. Ma, X. Gao, B. Q. Lv, L.-Y. Kong, Y.-B. Huang, P. Richard, M. Shi, V. N. Strocov, C. Fang, H.-M. Weng, Y.-G. Shi, T. Qian, and H. Ding, Dirac nodal surfaces and nodal lines in ZrSiS, Sci. Adv. **5**, eaau6459 (2019).
[55] C. C. Gu, J. Hu, X. L. Chen, Z. P. Guo, B. T. Fu *et al.*, Experimental evidence of crystal symmetry protection for the topological nodal line semimetal state in ZrSiS, Phys. Rev. B **100**, 205124 (2019).
[56] M. Neupane, I. Belopolski, M. M. Hosen, D. S. Sanchez, R. Sankar, M. Szlawska, S.-Y. Xu, K. Dimitri, N. Dhakal, P. Maldonado, P. M. Oppeneer, D. Kaczorowski, F. Chou, M. Z. Hasan, and T. Durakiewicz, Observation of topological nodal fermion semimetal phase in ZrSiS, Phys. Rev. B **93**, 201104(R) (2016).
[57] X. Wang, X. Pan, M. Gao, J. Yu, J. Jiang, J. Zhang, H. Zuo, M. Zhang, Z. Wei, W. Niu, Z. Xia, X. Wan, Y. Chen, F. Song, Y. Xu, B. Wang, G. Wang, and R. Zhang, Evidence of both surface and bulk Dirac bands and anisotropic nonsaturating magnetoresistance in ZrSiS, Adv. Electron. Mater. **2**, 1600228 (2016).
[58] M. M. Hosen, K. Dimitri, I. Belopolski, P. Maldonado, R. Sankar, N. Dhakal, G. Dhakal, T. Cole, P. M. Oppeneer, D. Kaczorowski, F. Chou, M. Z. Hasan, T. Durakiewicz, and M. Neupane, Tunability of the topological nodal-line semimetal phase in ZrSiX-type materials (X = S, Se, Te), Phys. Rev. B **95**, 161101(R) (2017).
[59] C. Chen, X. Xu, J. Jiang, S.-C. Wu, Y. P. Qi *et al.*, Dirac line nodes and effect of spin-orbit coupling in the nonsymmorphic critical semimetals MSiS(M = Hf, Zr), Phys. Rev. B **95**, 125126 (2017).
[60] R. Singha, A. K. Pariari, B. Satpati, and P. Mandal, Large nonsaturating magnetoresistance and signature of nondegenerate Dirac nodes in ZrSiS, Proc. Natl. Acad. Sci. U.S.A. **114**, 2468 (2017).
[61] See Supplemental Material at http://link.aps.org/supplemental/10.1103/PhysRevLett.127.186802 for details about material preparations, experimental methods, temperature-dependent HREELS data, and calculations, which includes Refs. [62–69].
[62] Y. Lv, B. Zhang, X. Li, S. Yao, Y. B. Chen, J. Zhou, S.-T. Zhang, M. Lu, and Y. Chen, Extremely large and significantly anisotropic magnetoresistance in ZrSiS single crystals, Appl. Phys. Lett. **108**, 244101 (2016).
[63] H. Raether, *Excitation of Plasmons and Interband Transitions by Electrons* (Springer-Verlag, Berlin/Heidelberg, 1980), Vol. 88, https://doi.org/10.1007/BFb0045951.
[64] *Vibrational Spectroscopy of Adsorbates*, edited by V. I. Goldanskii, R. Gomer, F. P. Schäfer, J. P. Toennies, and R. F. Willis (Springer Berlin Heidelberg, Berlin, Heidelberg, 1980), Vol. 15, https://doi.org/10.1007/978-3-642-88644-7.
[65] P. Laitenberger and R. E. Palmer, Plasmon Dispersion and Damping at the Surface of a Semimetal, Phys. Rev. Lett. **76**, 1952 (1996).
[66] Y. Liu, R. F. Willis, K. V. Emtsev, and T. Seyller, Plasmon dispersion and damping in electrically isolated two-dimensional charge sheets, Phys. Rev. B **78**, 201403(R) (2008).
[67] T. Rauch, T. Olsen, D. Vanderbilt, and I. Souza, Geometric and nongeometric contributions to the surface anomalous hall conductivity, Phys. Rev. B **98**, 115108 (2018).
[68] M. Rocca, Low-energy EELS investigation of surface electronic excitations on metals, Surf. Sci. Rep. **22**, 1 (1995).
[69] R. Ritchie and A. Marusak, The surface plasmon dispersion relation for an electron gas, Surf. Sci. **4**, 234 (1966).
[70] A. Topp, R. Queiroz, A. Grüneis, L. Müchler, A. W. Rost, A. Varykhalov, D. Marchenko, M. Krivenkov, F. Rodolakis, J. L. McChesney, B. V. Lotsch, L. M. Schoop, and C. R. Ast, Surface Floating 2D Bands in Layered Nonsymmorphic Semimetals: ZrSiS and Related Compounds, Phys. Rev. X **7**, 041073 (2017).
[71] X. Zhu, Y. Cao, S. Zhang, X. Jia, Q. Guo, F. Yang, L. Zhu, J. Zhang, E. W. Plummer, and J. Guo, High resolution electron energy loss spectroscopy with two-dimensional energy and momentum mapping, Rev. Sci. Instrum. **86**, 083902 (2015).
[72] S. Xue, T. Zhang, C. Yi, S. Zhang, X. Jia, L. H. Santos, C. Fang, Y. Shi, X. Zhu, and J. Guo, Electron-phonon coupling and Kohn anomaly due to floating two-dimensional electronic bands on the surface of ZrSiS, Phys. Rev. B **100**, 195409 (2019).
[73] E. T. Jensen, R. E. Palmer, W. Allison, and J. F. Annett, Temperature-Dependent Plasmon Frequency and Linewidth in a Semimetal, Phys. Rev. Lett. **66**, 492 (1991).
[74] R. Y. Chen, S. J. Zhang, J. A. Schneeloch, C. Zhang, Q. Li, G. D. Gu, and N. L. Wang, Optical spectroscopy study of the three-dimensional Dirac semimetal $ZrTe_5$, Phys. Rev. B **92**, 075107 (2015).
[75] Note that the interband correlations between the bulk bands is negligible because of the domination of the intraband correlations in metal over the interband correlations; and the interband correlations between the bulk states and the surface states does not manifest because of their weak overlap.
[76] H. Ibach and D. L. Mills, *Electron Energy Loss Spectroscopy and Surface Vibrations* (Academic Press, New York, 1982), https://doi.org/10.1016/C2013-0-10894-X.
[77] G. Giuliani and G. Vignale, *Quantum Theory of the Electron Liquid* (Cambridge University Press, Cambridge, England, 2005).
[78] Experiments suggested that the spin-orbit coupling (SOC) gap does not significantly modify the nodal line structure in

ZrSiS [54,55]. We thus neglecte the SOC effect in the calculations of plasmon dispersions.

[79] K.-D. Tsuei, E. Plummer, A. Liebsch, E. Pehlke, K. Kempa, and P. Bakshi, The normal modes at the surface of simple metals, Surf. Sci. **247**, 302 (1991).

[80] T. Stauber, Plasmonics in Dirac systems: From graphene to topological insulators, J. Phys. Condens. Matter **26**, 123201 (2014).

[81] S. Cong, X. Liu, Y. Jiang, W. Zhang, and Z. Zhao, Surface enhanced Raman scattering revealed by interfacial charge-transfer transitions, The Innovation **1**, 100051 (2020).